Evaluating the Representation of Arctic Cirrus Solar Radiative Effects in the IFS with Airborne Measurements

Johannes Röttenbacher[1], André Ehrlich[1], Hanno Müller[1], Florian Ewald[2], Anna E. Luebke[1], Benjamin Kirbus[1], Robin J. Hogan[3], and Manfred Wendisch[1]

[1]Leipzig Institute for Meteorology, Leipzig University, 04013 Leipzig, Germany
[2]Deutsches Zentrum für Luft- und Raumfahrt, Institut für Physik der Atmosphäre, Oberpfaffenhofen, Germany
[3]European Centre for Medium-Range Weather Forecasts, Reading, United Kingdom

Correspondence: Johannes Röttenbacher (johannes.roettenbacher@uni-leipzig.de)

Abstract. In this case study, measured solar irradiances above and below Arctic cirrus are compared to simulations of the European Centre for Medium-Range Weather Forecasts' Integrated Forecasting System (IFS) making use of offline runs of the operational ecRad radiation scheme. Independent of the solar irradiances, cirrus properties are derived from active remote sensing and used to evaluate the optical and microphysical parameterizations in ecRad. The data set was collected in the central

5   Arctic over sea ice (81° - 90° North) with the High Altitude LOng range research aircraft (HALO) during a campaign in March and April 2022. HALO was equipped with broadband radiation and remote sensing instrumentation, including upward and downward-looking pyranometers (solar irradiance), a cloud radar, and a multi-wavelength water vapor differential absorption lidar. Flight legs above and below single-layer cirrus were performed. Measurements of solar irradiance are used to evaluate the ecRad radiation scheme in two case studies of optically thin and thick cirrus. The optically thin cirrus had a mean transmissivity

10   of 0.9, while the optically thick cirrus had a transmissivity of about 0.6. Different ice optics parameterizations optionally available within ecRad are tested to improve the match between simulation and measurements. Furthermore, the IFS predicted ice water content and ice effective radius were replaced by values retrieved with the radar and lidar. The choice of ice optics parameterizations does not significantly improve the model-measurement agreement. However, introducing the retrieved ice microphysical properties brings measured and modelled irradiances into closer agreement for the optical thin cirrus, while the

15   optically thick cirrus case is now simulated as too thick. From the comparison of the different ice optics parametrizations in the original and in the forced setup, it can be concluded that the ice water content forcasted by the IFS is realistic. The missmatch between observed and simulated irradiances mostly originates from the assumed or parameterized ice effective radius.

1 Introduction

Cirrus play an important part in the radiative budget of the Arctic atmosphere (Hong and Liu, 2015). Their total radiative
effect is determined by the balance of a solar warming and a terrestrial cooling effect. In the terrestrial spectrum, cirrus warm
the atmosphere below the cloud layer as they absorb most of the upward terrestrial radiation emitted by the surface and the
atmosphere below the cloud but usually emit at a lower temperature than the surface. This warming can be offset by the
reflectance of incoming solar radiation at cloud top. The balance between reflected and transmitted solar radiation depends
on the optical thickness of the cloud (Liou, 1986; Lynch, 2002). Ice crystal shape also plays an important role especially for
optically thin cirrus where single scattering processes dominate (Wendisch et al., 2005, 2007; Eichler et al., 2009; Baran, 2012).

The radiative effect of Arctic cirrus, which we define to occur north of the Arctic circle at $66°$ N, exhibits specific dependen-
cies on the high gradients of surface albedo and the usually low sun. During polar night no sunlight is present in the Arctic, and
thus, cirrus always warms the atmosphere below it (Hong and Liu, 2015). However, the magnitude of this warming depends
on the surface temperature and the emissivity of the surface. The temperature and emissivity of the Arctic ocean surface can
be very heterogeneous depending on the sea ice cover and amount and size of leads and melt ponds, which vary as a function
of season and latitude (Light et al., 2022). During polar day, the solar radiative effect of Arctic cirrus becomes more important.
However, the solar zenith angle is still large leading to longer paths of the incoming radiation through the cirrus and to more
complex scattering geometries and increasingly important 3D radiative effects such as upward and downward trapping and
escape due to horizontal photon transport (Várnai and Davies, 1999).

Due to their influence on the radiative energy budget in the Arctic (Marsing et al., 2023), cirrus need to be properly repre-
sented in numerical weather prediction (NWP) models. One important component of each NWP model considers the atmo-
spheric radiative transfer, calculating the radiative energy budget and atmospheric heating and cooling rates as a driver for
dynamic processes. For these calculations, the radiative properties of cirrus need to be input to the solver. However, espe-
cially the radiative properties of ice clouds are difficult to represent in such radiative transfer models due to the complexity
of microphysical properties of ice crystals (Wolf et al., 2018; Lawson et al., 2019) and complex shape effects (Baran, 2012).
Thus, the optical properties of ice clouds are parameterized in NWP models as a function of available prognostic variables,
such as temperature and ice water content (IWC) (Fu, 1996; Fu et al., 1998; Yi et al., 2013; Baran et al., 2014, 2016). These
parameterizations are developed by simulating scattering and absorption properties of ice crystals of different shapes and sizes
(Yang et al., 2014). Together with particle size distributions (PSDs) derived from in situ aircraft measurements, bulk optical
properties of clouds are derived and applied in the radiation scheme (Ebert and Curry, 1992).

The Integrated Forecasting System (IFS) operated by the European Centre for Medium-Range Weather Forecasts (ECMWF)
uses the radiation scheme ecRad (Hogan and Bozzo, 2018). ecRad calculates the radiative flux densities (irradiances) in 14
solar wavelength bands using a two-stream solver. The radiative transfer through cirrus is simulated utilizing the ice optics
parameterization developed by Fu (1996) for the solar bands. The parameterization for the solar radiative properties uses
in situ measurements of ice crystal size distributions from 28 flights in the mid-latitudes and tropics. No data from Arctic
cirrus is included. Assuming hexagonal ice crystals, Fu (1996) defines a generalized effective size (D_{ge}) and IWC as the

only two input parameters. Based on that, they parameterize the wavelength dependent single scattering properties (extinction coefficient, single scattering albedo, asymmetry parameter). They show that D_{ge} relates to the total cross-sectional area of ice particles per unit volume, which makes the parameterization of the extinction coefficient and the single scattering albedo independent of particle shape. Thus, they conclude that the parameterization is suitable for the application in global climate models. However, it is also mentioned that the asymmetry parameter is sensitive to the particle shape, which is not considered in this parameterization. Further studies showed that the surface roughness of ice crystals also plays an important role for their optical properties, especially for the scattering phase function and the asymmetry parameter (Eichler et al., 2009; Tang et al., 2017; Järvinen et al., 2018). The implementation of an optimized parameterization of the asymmetry parameter is, therefore, still an ongoing process in terms of the IFS's treatment of radiative transfer through cirrus.

The ice optics parameterization defined by Fu (1996) depends on the IWC and the cross-sectional area of the ice particles per unit volume (quantified by D_{ge}). However, only the IWC is a prognostic variable in global models such as the IFS. Therefore, a parameterization of D_{ge} is required. Fu (1996) showed that D_{ge} can be related to the ice effective radius (r_{eff}) defined by Foot (1988) and Francis et al. (1994). This relation is applied by Sun and Rikus (1999) to parameterize r_{eff} as a function of IWC and temperature using the ice crystal size distribution parameterization from McFarquhar and Heymsfield (1997). To evaluate the parameterization Sun and Rikus (1999) used it together with the parameterization by Fu (1996) to simulate the irradiances for two mid-latitudinal case studies, for which in situ measurements of irradiances and D_{ge} are available. Comparing the simulations and observations yields reasonable agreement mostly within the measurement uncertainty. After comments by McFarquhar (2001), Sun (2001) revised the parameterization to account for a singularity. The resulting parameterization of r_{eff} together with the ice optics parameterization by Fu (1996) has been used within the IFS since 2007 (Hogan and Bozzo, 2018).

The prospects for ice optics parameterizations increased in recent years due to the availability of increasingly complex scattering models (Yang et al., 2014) and more powerful computers. Furthermore, more in situ measurements of ice crystal particles in cirrus at different altitudes, latitudes and temperatures became available (Baran, 2012; Luebke et al., 2013; Krämer et al., 2020). However, only few in situ measurements of ice crystals in the Arctic have been reported. De La Torre Castro et al. (2023) analyzed in situ measurements of ice particles from the Cirrus in High Latitudes (CIRRUS-HL) aircraft campaign, which took place in June and July 2021. A limited number of flights ($7.8\,\mathrm{hours}$ within cirrus north of $60°\,\mathrm{N}$, defined as high-latitude) provided valuable data sets for case studies. The authors compared mid- and high-latitude cirrus with respect to the ice crystal number concentration, mean effective diameter and IWC. They found that cirrus formed and measured in the high-latitudes have a lower ice crystal number concentration and a larger ice effective diameter compared to cirrus formed in the mid-latitudes, which are commonly used to derive the ice optics parameterizations cited above.

It is therefore important to test the capabilities of the current IFS simulations to realistically represent the influence of cirrus on solar radiative transfer in the Arctic. One approach to evaluate the performance of the IFS, and ecRad in particular, has been shown by Wolf et al. (2020) and Müller et al. (2023), who used airborne observations of solar irradiance and remote sensing data to evaluate the representation of ice-topped clouds over the North Atlantic and Arctic low-level clouds, respectively. Here, we build on this method to quantify the performance of ecRad concerning Arctic cirrus. To separate the possible sources of uncertainties in the simulations, we utilize a microphysical retrieval of cirrus properties to perform sensitivity studies with

respect to the predicted IWC by the IFS. The aircraft campaign, instruments and measurements used in this study are introduced in Sect. 2. In Sect. 3, the setup of the radiative transfer simulations and the evaluation strategy is explained. The results of the evaluation are presented in Sect. 4 followed by a summary and conclusions in Section 5.

90 ## 2 Airborne observations of Arctic cirrus

2.1 Measurements

Evaluating the performance of ecRad with respect to Arctic cirrus requires direct measurements of the radiative budget above and below cloud. In the remote central Arctic, such measurements were collected by the High Altitude LOng range research aircraft (HALO) during the recent HALO-(AC)[3] (ArctiC Amplification: Climate Relevant Atmospheric and SurfaCe Processes,
95 and Feedback Mechanisms) campaign. HALO was stationed in Kiruna, Sweden and conducted 18 research flights between March and April 2022 into the Fram Straight and over the central Arctic Ocean. HALO was configured with its cloud observatory payload (Stevens et al., 2019) including the WAter vapor Lidar Experiment in Space (WALES, Wirth et al., 2009) and the HALO Microwave Package radiometer system (HAMP, Mech et al., 2014), including a 35 GHz cloud radar. For measurements of atmospheric temperature and humidity profiles, numerous dropsondes were released. To measure the upward and
100 downward broadband irradiance HALO was equipped with the Broadband AirCrAft RaDiometer Instrumentation (BACARDI, Ehrlich et al., 2023), which consists of two sets of Kipp & Zonen CMP22 pyranometers and CGR4 pyrgeometers. They measure irradiances in the solar $(0.3 - 3\,\mu m)$ and terrestrial $(3 - 100\,\mu m)$ wavelength range. For this study the solar irradiance measurements were analyzed.

The data processing of the pyranometer including corrections for the sensor sensitivity, thermal dynamic offsets, sensor
105 inertia and aircraft attitude are described by Ehrlich et al. (2023), who also discuss the measurement uncertainties of the pyranometers. For operation in high latitudes with low ambient temperature conditions such as during HALO-(AC)[3], the temperature dependency of the sensor sensitivity has to be considered. During HALO-(AC)[3] ambient temperatures around $-55\,°C$ were common at flight altitude, exceeding the calibration certificate by the manufacturer. Therefore, the uncertainty of the measured irradiances is higher than reported by Ehrlich et al. (2023).

110 Additionally, the large solar zenith angles (low sun) pose another challenge in high latitudes. Uncertainties due to the imperfect angular response of the pyranometers reach up to $1\,\%$ for solar zenith angles larger than $80°$ (Ehrlich et al., 2023) and the correction of the aircraft attitude introduces additional uncertainties (Wendisch et al., 2001). Similar to Ehrlich et al. (2023), the performance of BACARDI during HALO-(AC)[3] was evaluated against cloud-free radiative transfer simulations. For the solar downward irradiance measured at altitudes of $10\,km$ and higher the uncertainties are estimated with about $\pm 5\,\%$.

115 ### 2.2 Case study

For the interpretation of the radiative properties of cirrus, a cloud-free atmosphere below the cirrus is advantageous because the effect of the cirrus and low clouds are hard to distinguish otherwise. During HALO-(AC)[3] research flight (RF) 17 on 11

April 2022 and RF 18 on 12 April 2022 fulfilled these conditions of a single layer cirrus. The tracks of the two flights together with the respective high cloud cover and the sea ice edge as predicted by the IFS $0\,\mathrm{UTC}$ run from 11 and 12 April 2022 are shown in Fig. 1. The flight sections of the analyzed cases are highlighted in orange in the far north of the flight track. Along each of those flight legs remote sensing measurements were performed above and below cirrus.

Both cases happened under similar synoptic conditions. On 09 April 2022, a low pressure system over Scandinavia advected warm and moist air into the Fram Strait. Due to a convergence with a cold air mass that had its origin in Greenland, a vertical wind shear developed with low-level northeasterly winds and southeasterly winds at levels above $700\,\mathrm{hPa}$. This southeasterly flow transported the initial moisture of the observed cirrus into the central Arctic. Due to a cold air outflow from the Greenland ice sheet into the central Arctic, the northbound air mass had to slowly ascend and formed the isolated cirrus with no low level clouds below. The backward trajectories ending in the observed location and altitude of the cirrus shown in Fig. 1 were calculated with the Lagrangian analysis tool (LAGRANTO, Sprenger and Wernli, 2015) based on data from the fifth version of the ECMWF's atmospheric reanalysis (ERA5, Hersbach et al., 2020). The trajectories indicate that the majority of the air mass featuring the cirrus was transported from the south into the central Arctic. Some of the air mass featuring the cirrus on 11 April 2022 also originated in the eastern central Arctic. On 12 April 2022 the whole sampled air mass came with the poleward moisture transport through the Fram Strait. The IFS high cloud cover (shown as blue shading in Fig. 1) indicates that the observed cirrus was part of a larger cirrus field. In combination with the uniform shape of the trajectories, this suggests that the observations are representative for this cirrus field and cirrus properties can be assumed to be stable during the one hour flight pattern. Due to the large scale lifting of the air mass, the cirrus is rather homogeneous on a large scale. This justifies the combination of observations of the above-cloud and below-cloud flight legs, which are separated by about 15 minutes. However, on a smaller scale, horizontal heterogeneities were present.

2.3 Cirrus radiative properties

Figure 2 shows solar broadband irradiance measurements of the above and below-cloud section from RF 17 and RF 18 along the flight track. Data has been filtered for aircraft attitude changes during turns, descents, and ascents. The transmissivity of the cloud is calculated as the ratio between the below-cloud measurements and the ecRad cloud-free simulations at around $11\,\mathrm{km}$. To facilitate understanding, the x-axis shows the distance traveled by HALO from the start to the end of the above-cloud section. The two flights show distinctively different structures in the measurements owing to the different flight patterns. In Fig. 2 (a) the straight flight leg towards the northwest and the corresponding increase in the solar zenith angle from $77.6°$ to $79.8°$ is reflected in the decrease in solar downward irradiance from $250\,\mathrm{Wm^{-2}}$ to $225\,\mathrm{Wm^{-2}}$. During the pentagon flight pattern in RF 18 the solar zenith angle was generally larger than $79°$ and thus changed less than during RF 17. This results in a lower average solar downward irradiance of $206\,\mathrm{Wm^{-2}}$ for RF 18 compared to $238\,\mathrm{Wm^{-2}}$ for RF 17. The below-cloud measurements reveal high variability in the transmissivity which is linked to the optical depth of the cirrus. In RF 17 the downward solar irradiance varied with a standard deviation of $16\,\mathrm{Wm^{-2}}$ corresponding to a change of transmissivity between $0.69 - 0.93$. The cirrus in RF 18 showed slightly less variability ($11\,\mathrm{Wm^{-2}}$ standard deviation) and was less transmissive ($0.49 - 0.71$).
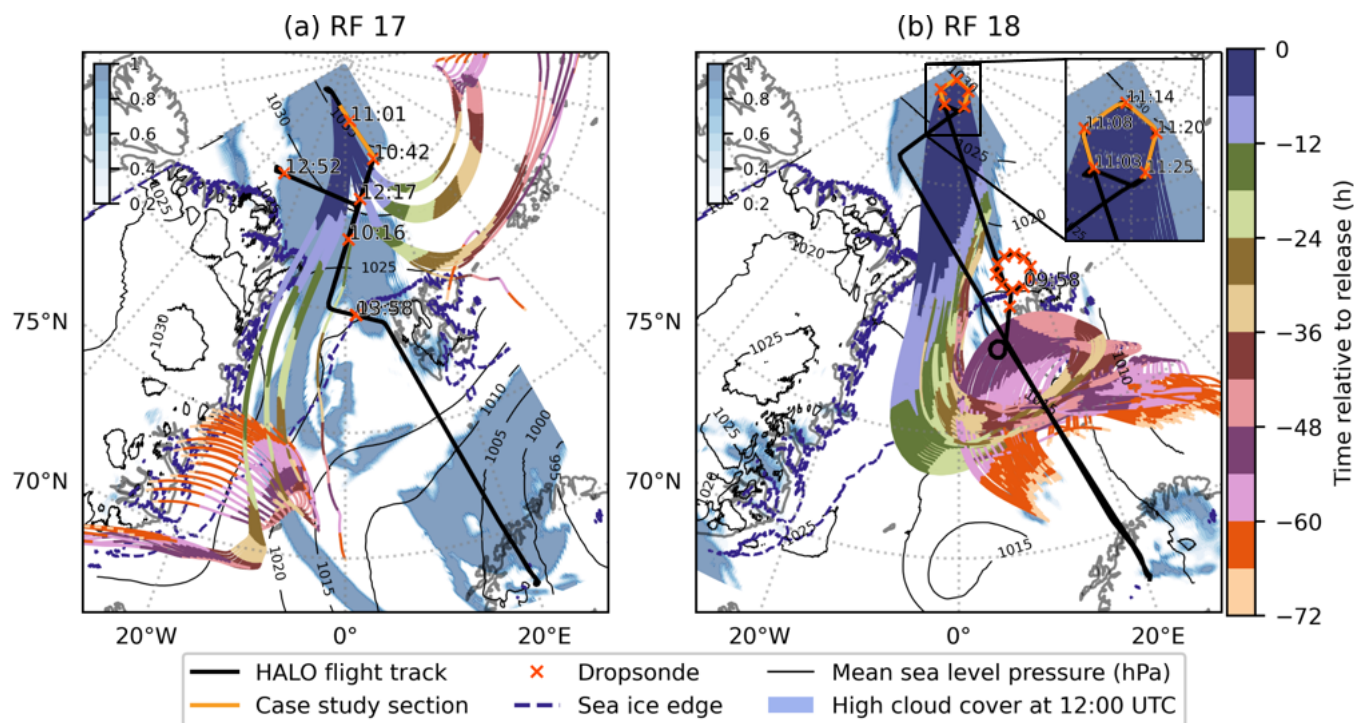
Figure 1. Map of flight tracks with IFS predicted high cloud cover for 12 UTC , sea ice edge (80 % sea ice cover), mean sea level pressure isolines, dropsonde locations (red crosses), highlighted case study regions (orange), and LAGRANTO backward trajectories for (a) RF 17 and (b) RF 18. The box in panel (b) shows a zoom of the case study region with the above and below-cloud flight sections for RF 18.

3 Evaluation strategy for the IFS and ecRad

3.1 IFS and ecRad setup

The airborne observations are used to evaluate the IFS of the ECMWF. The solar broadband irradiances are compared with the
155 simulations of the radiation scheme ecRad. The IFS forecast is fed into version 1.5.0 of ecRad, which is run in an offline mode to allow for sensitivity studies by exchanging specific IFS forecast variables and vary the applied ice optics parameterization. This approach is adapted from Wolf et al. (2020) and Müller et al. (2023). Instead of the operational Monte Carlo integration of the Independent Column Approximation (McICA, Pincus et al., 2003), the Speedy Algorithm for Radiative Transfer through Cloud Sides (SPARTACUS, Hogan et al., 2016; Schäfer et al., 2016) is used as a solver because it provides the spectral
160 irradiances at all model levels and has tools available to parameterize 3D radiative effects. The spectral resolution of the ecRad simulations depends on the chosen gas absorption model, which in this study is the Rapid Radiative Transfer Model for General Circulation Models (RRTM-G, Mlawer et al., 1997).

We employ the IFS data from the operational octahedral reduced Gaussian grid (O1280) based on the IFS cycle 47R1 with 137 vertical levels. The hourly IFS forecast initialized at 0 UTC of the corresponding flight day is used, and all relevant input
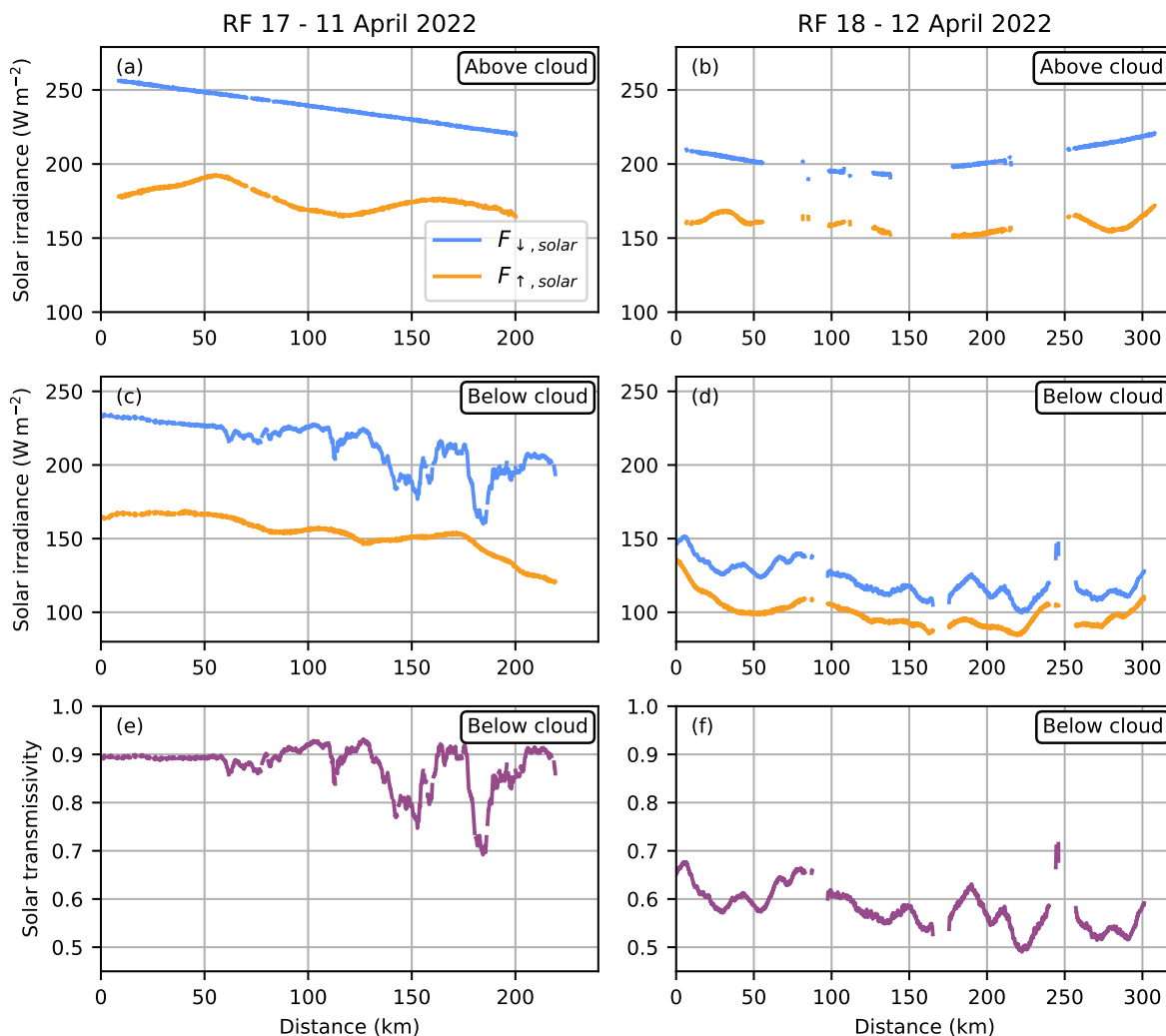
Figure 2. Measured downward and upward solar irradiance from BACARDI for the (a, b) above and (c, d) below-cloud sections of (a, c) RF 17 and (b, d) RF 18. Panels (e) and (f) show the solar transmissivity below cloud. The x-axis shows the distance traveled by HALO from the start to the end of the above-cloud section.

165 variables for ecRad are extracted along the flight path of HALO. One problem that needs to be accounted for is the scale mismatch between the measurements and the model output. The BACARDI irradiance measurements are recorded at $10\,Hz$ time resolution resulting in a measurement every $20\,m$ assuming an average aircraft speed of $200\,m\,s^{-1}$ for HALO. Although BACARDI samples the whole hemisphere, $95\,\%$ of the signal stem from a footprint of about $500\,km^2$ at $3\,km$ distance from the target, which is the approximate flight altitude above cirrus for the case studies. The characteristic length scale of the IFS

170 in the Arctic varies slightly between $8\,km$ and $9.5\,km$. Therefore, the measurements are averaged to one minute resolution to match the spatial resolution of one IFS grid cell. For the same reason, simulations are performed every minute along the flight track.

Regarding the time mismatch, the IFS data is not averaged between time steps as this would assume a linear change for all model parameters, which might be true for some but certainly not for all quantities such as relative humidity and IWC.

175 This results in a maximum offset of $30\,minutes$ between any measurement and the next closest forecast time step. For the case studies presented here this means that the above-cloud sections are covered by the $11\,UTC$ time step and the below-cloud sections are covered by the $12\,UTC$ time step, with the switch happening either during the descent to the below-cloud section or just afterwards. The solar zenith angle is set to the time and location of HALO for each ecRad simulation step. To account for a possible slight offset of the location of the clouds between model and measurement, the ten closest grid points to the

180 flight path are selected, covering a circular area between $616\,km^2$ and $1050\,km^2$. The same solar zenith angle is used for the simulation of the ten closest grid points.

For the trace gases CFC-11, CFC-12, CO_2, CH_4, N_2O and O_3 a monthly mean climatology is used depending on latitude and pressure level. The climatology is based on the reanalysis produced by the Monitoring Atmospheric Composition and Climate project (MACC, Inness et al., 2013) for CO_2 and CH_4, the Cariolle model (Cariolle and Déqué, 1986; Cariolle

185 and Teyssèdre, 2007) for CFC-11, CFC-12 and N_2O, and the Copernicus Atmospheric Monitoring Service (CAMS) Interim reanalysis (Flemming et al., 2017) for O_3. The incoming solar irradiance at top of atmosphere is also prescribed in the simulations using a value of $1360.8\,Wm^{-2}$ provided by Kopp and Lean (2011) and is adjusted for the Earth-Sun-distance at noon of each flight day. To keep the focus on the cloud properties, aerosol particles are turned off in the simulations. A detailed Fortran namelist with all options and an example input file is available in the GitHub repository accompanying this paper

190 (https://github.com/radiation-lim/roettenbacher_etal_2024, last accessed 02.02.2024).

3.2 Surface albedo parameterization

In the operational mode, when ecRad is run within IFS, the IFS host system provides the surface albedo. In the offline mode that is used here, this parameter has to be provided. Therefore, following the operational setup, the surface albedo along the flight track is calculated by combining an open ocean albedo with the sea ice albedo parameterization by Ebert and Curry

195 (1993). The two albedo values are thereby weighted according to the IFS predicted sea ice fraction. A further differentiation of the ocean albedo is made by using the solar zenith angle dependent parameterization from Taylor et al. (1996) for the direct solar surface albedo, while the diffuse solar surface albedo is fixed to a value of 0.06. The ocean albedo is assumed to be constant with wavelength, while the sea ice albedo parameterization provides a monthly mean value for six solar bands. For the

winter months, the IFS assumes the surface albedo for dry snow and for the summer months the albedo of bare ice according
200   to Ebert and Curry (1993). Although the case studies appeared in April we still follow the assumptions for the winter months
as the central Arctic wasn't affected by thawing during the case studies. Thus, the assumption of bare ice is not yet justified.

3.3   Ice optics parameterizations

The choice of ice optics parameterization is crucial to simulate the Earth's radiative energy budget (Fu, 2007; Baran, 2012; Yi,
2022). With ecRad it is possible to switch between different parameterizations including the operational one from Fu (1996)
205   (referred to as Fu-IFS), the one based on Yi et al. (2013) (referred to as Yi2013), and the most recent one by Baran et al. (2016)
(referred to as Baran2016). The relevant details of the three parameterizations are summarized in Table 1. In general, all three
parameterizations derive the bulk optical properties of a grid cell as a function of IWC and temperature. However, Fu-IFS and
Yi2013 do not use temperature directly but instead need r_{eff} as an explicit input. Thus, r_{eff} is calculated in the operational mode
of the IFS using the parameterization from Sun (2001). To account for the observation that ice crystals are generally larger in
210   the tropics than in the mid-latitudes (Field et al., 2007), the minimum r_{eff} predicted by the Sun (2001) parameterization is
scaled with the cosine of the latitude. Due to the lack of in situ observations in the Arctic, this parameterization with latitude is
extrapolated for high latitudes.

Baran2016, on the other hand, parameterize the bulk optical properties directly as a function of IWC and in-cloud tem-
perature. Another difference to Fu-IFS and Yi2013 is the use of synthetic PSDs derived from the parameterization by Field
215   et al. (2007). By that, the temperature range of the parameterization is extended down to -80° C, and the diagnostic r_{eff} is not
needed in the parameterization. Apart from the difference in input variables, the parameterizations are also based on different
sets of in situ cirrus observations and assume different ice habits and mixtures (see Table 1).

3.4   VarCloud retrieval

To independently validate the prognostic IWC and the diagnostic r_{eff} used in the ice optics parameterizations, active remote
220   sensing measurements from HALO are applied. Using synergistic radar and lidar measurements from HALO, the IWC and
r_{eff} are retrieved using a technique developed by Ewald et al. (2021). The retrieval is based on a variational optimal estimation
algorithm (VarCloud, Delanoë and Hogan, 2008). The algorithm iterates forward simulations of radar and lidar reflectivity until
convergence between the simulated and measured signals is reached. The first guess of the cloud properties is provided using
the radar-lidar mask with climatological profiles of number concentration and lidar ratio which are a function of temperature
225   (Cazenave et al., 2019). The lidar backscatter is then calculated using the forward model developed by Hogan (2008) and look
up tables of T-matrix (Mishchenko et al., 1996) calculations of soft spheroids for the radar backscatter. The forward simulations
assume a constant relationship between the ice crystal mass M and the volume of a sphere that encloses the maximum diameter
D_{max} of the ice particle following the most recent update of the "composite" M-D_{max} relationship by Cazenave et al. (2019).
The particle shape is modeled as horizontally aligned oblate spheroids following Hogan et al. (2012). Following the approach
230   by Delanoë et al. (2005), a normalized PSD is used. By integrating the visible extinction cross-section, which is approximated
by two times the geometric cross-section, and the radar cross-section over this PSD, the visible extinction and radar reflectivity

Table 1. Main differences between the three available ice optics parameterizations in ecRad.

Name	Particle size distributions	Ice crystal habit assumption	Input variables
Fu-IFS	28 from mid-latitudes and tropics	randomly oriented hexagonal ice crystals	IWC and ice crystal effective radius
Yi2013	14 408 from 11 field campaigns (Heymsfield et al., 2013)	nine habits with a rough surface from a general habit mixture dependent on maximum diameter (droxtals, solid and hollow bullet rosettes, solid and hollow columns, plates, aggregate of solid columns, small and large aggregate of plates) (Baum et al., 2011)	IWC and ice crystal effective radius
Baran2016	Synthetic PSDs using 20 662 combinations of IWC and in-cloud temperature using the parameterization developed by (Field et al., 2007) based on 14 000 PSDs	ensemble model of six ice crystal habits dependent on maximum dimension (hexagonal ice column, 6-branched bullet rosette, 3-, 5-, 8- and 10- monomer ice aggregates (Baran and Labonnote, 2007)	IWC and temperature

are obtained. IWC is retrieved in the same way using the ice crystal mass. From these values, r_{eff} is calculated using the relationship between IWC and visible extinction coefficient derived by Foot (1988). The product provides profiles of r_{eff} and IWC of cirrus along the flight track at a 1 second time resolution (~200 m horizontal) and 30 m vertical resolution when the aircraft was above cloud.

4   Results

4.1   Cirrus representation in the IFS

Before comparing solar broadband irradiances, the general representation of the synoptic condition and the cirrus in the IFS numerical weather forecast are evaluated by dropsonde and remote sensing observations from HALO. One cause of uncertainty in the representation of cirrus can be an incorrect prediction of the atmospheric state in the IFS. Fig. 3 shows the atmospheric temperature and humidity profiles from the IFS forecast for the case study period (above and below-cloud section) and the ones measured by the dropsondes released during the above-cloud sections of the two flights. It has to be mentioned that the IFS did assimilate the dropsondes of the previous flights. While no flight (no dropsondes) was performed the day before RF 17, the dropsondes released during RF 17 might have affected the forecast for RF 18.

The deviations between the IFS and the dropsonde temperature profiles are minor and only reach up to 6 K close to the boundary-layer inversion, where a slight mismatch of the inversion altitude is found. As can be seen from the temperature
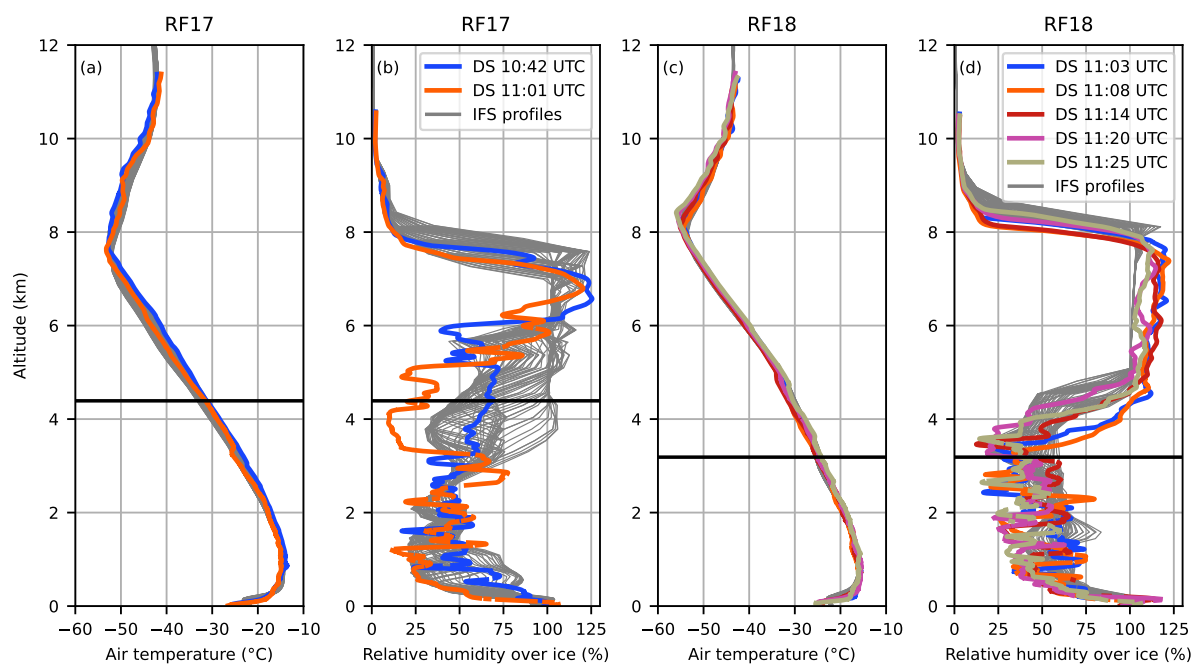
Figure 3. Atmospheric profiles of (a, c) air temperature and (b, d) relative humidity over ice from the IFS (grey lines) for the whole case study period (above and below-cloud section) along the flight track and the dropsondes (DS) deployed by HALO during the above-cloud section of (a, b) RF 17 and (c, d) RF 18. The black line indicates the flight altitude of HALO during the below-cloud section.

inversions at around $8\,\mathrm{km}$, HALO was well above the tropopause during both flights. The relative humidity (RH_{ice}) profiles indicate a high vertical variability both in the IFS and in the observations. While the height of the humidity drop at the tropopause matches, the humidity decrease at cloud base is more variable and slightly differs from the observations. This

250   strong decrease just at the tropopause means that the cirrus is capped by it. For RF 17, the IFS humidity profiles indicate a trend of decreasing cloud base along the flight track by showing higher values at lower altitudes. This is due to the cirrus thickening towards the end of the above-cloud section that is not fully captured by the dropsonde measurements. For RF 18, the layer of high humidity is more stable at cloud base (smaller flight area) but slightly higher than in the dropsonde observations. However, the model does not cover the full range of the measured RH_{ice}, especially below cloud. A very prominent feature

255   during RF 18 is that the model does not predict supersaturation with respect to ice inside the cirrus, which the dropsonde observes. This is due to the ice cloud scheme of the IFS, which allows for supersaturation with respect to ice in the clear sky portion of the grid cell but immediately converts supersaturation in the cloudy part into cloud ice thus limiting RH_{ice} to $100\,\%$. RF 17 does not feature many fully cloudy grid cells, and thus does not show this feature as prominent. The dropsondes show only a thin layer with RH_{ice} exceeding $100\,\%$. This indicates that a vertically thin cirrus was present during RF 17.

260   A more direct comparison of the cloud top and base altitude is achieved using radar and lidar measurements. Figure 4 shows the VarCloud lidar-radar cloud mask from HALO, the aircraft altitude, and the predicted cloud fraction of the IFS. It can be
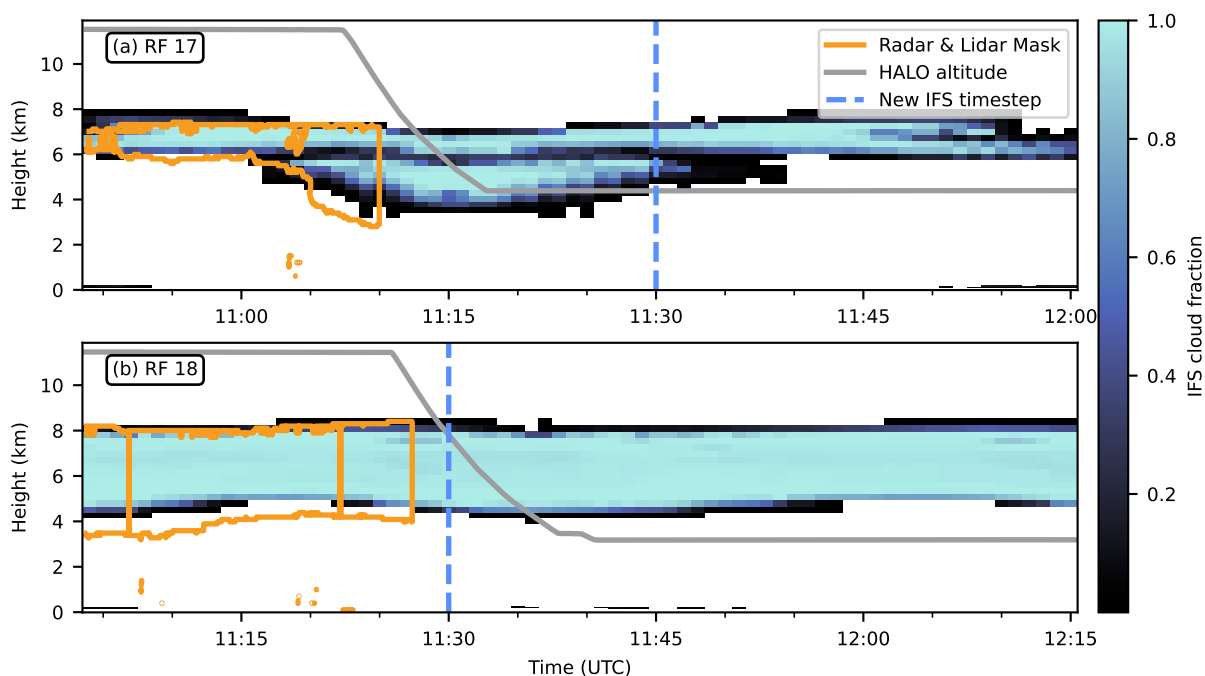
Figure 4. Comparison of lidar-radar cloud mask and IFS predicted cloud fraction for the case studies of (a) RF 17 and (b) RF 18.

seen that the IFS prediction mostly matches the actual location of the clouds in their vertical position. For RF 17, Fig. 4 (a), a slight overestimation of cloudiness can be seen at the beginning of the above-cloud section. Towards the end of the above-cloud section, the cloud becomes geometrically thicker earlier in the IFS than in the observations. However, it does not reach the same vertical extent as in the measurements. Thus, the below-cloud section started inside the lower part of the cirrus. However, these cloud layers were not visible by eye and can only be inferred from the radar signal. For the comparison and the simulations this part of the below-cloud section is excluded. Figure 4 (b) shows that the cloud in RF 18 extends to lower altitudes than predicted during the whole above-cloud section. Both flights also show a small amount of cloud particles close to the ground at the beginning of the above-cloud sections. The cloud fraction for these cloud layers only show values below 0.15, indicating thin clouds linked to the surface temperature inversion. However, these clouds were not captured by the radar or the lidar, nor by visual observations from the aircraft. Therefore, these cloud layers are removed from the IFS output for further analysis and the upcoming simulations.

The dashed vertical line in Fig. 4 (a) and (b) indicates the time when the IFS forecast switches from the 11 UTC to the 12 UTC time step. To quantify, how strong the cirrus field changed between the two time steps of the IFS, Fig. 5 shows the distribution of the IFS IWC at 11 UTC and at 12 UTC in the case study areas. RF 17 shows a shift towards smaller values from 11 UTC to 12 UTC, meaning that the cloud is dissolving or moving out of the case study area according to the IFS. For RF 18 no noteworthy differences can be seen between the 11 UTC and 12 UTC time step.
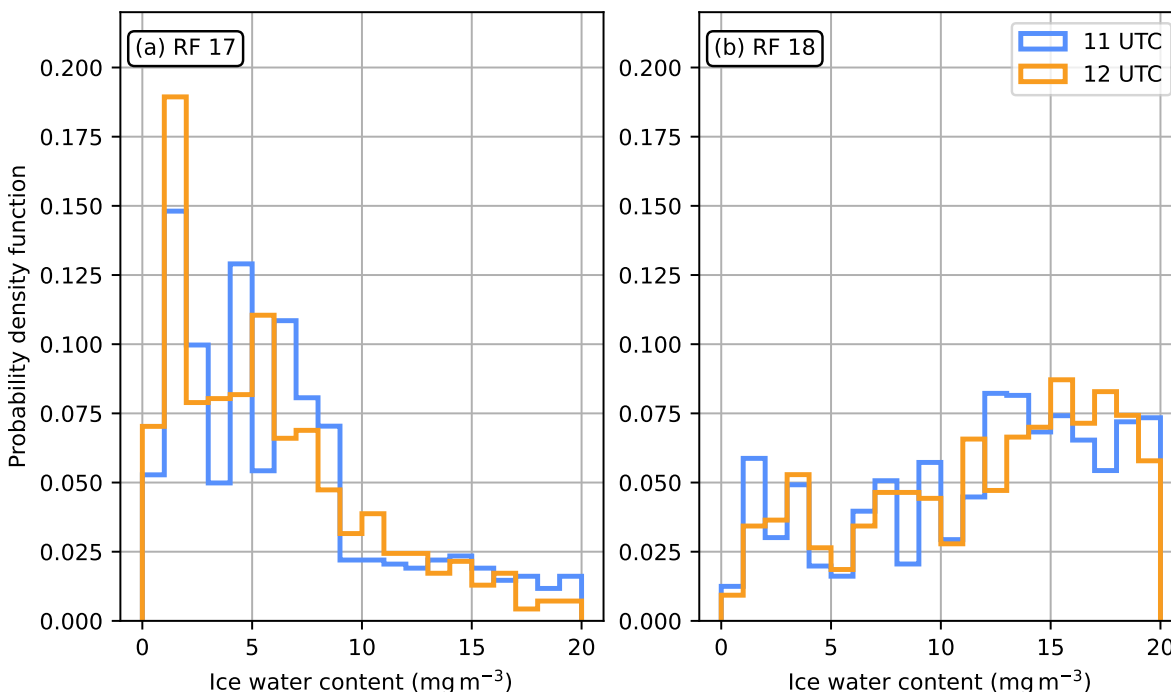
Figure 5. Probability density functions of the IWC for the 11 UTC and 12 UTC IFS time step for the IFS grid points in the case study areas of (a) RF 17 and (b) RF 18.

4.2 Comparisons of measured and simulated solar downward irradiance

Flight sections of cloud-free measurements above the aircraft can be used to validate the downward irradiance measurements.
280 Due to the lack of scattering and absorption by the remaining atmosphere above HALO, the radiative transfer simulations can be assumed to be precise. Remaining differences between simulation and measurement are assumed to stem from the instrument performance. Selected sections above $11\,\mathrm{km}$ of both RFs are compared and shown in Fig. 6. The validation shows a slight positive bias in the measurements and a small root mean square error of $3-5\,\mathrm{W\,m^{-2}}$, which is within the uncertainty range of BACARDI.

4.2.1 Ice optics parameterizations

To investigate the influence of the three chosen ice optics parameterization (see Table 1) two additional simulations are performed, in which only the ice optics parameterization is changed from the operational Fu-IFS to Yi2013 or Baran2016. The difference between those three simulations and the BACARDI measurements is best represented using probability density functions (PDFs) of the below-cloud section. Here, the corresponding solar transmissivity is calculated from the downward
290 irradiance above-cloud derived from simulations by ecRad and the below-cloud measurements of either BACARDI or the
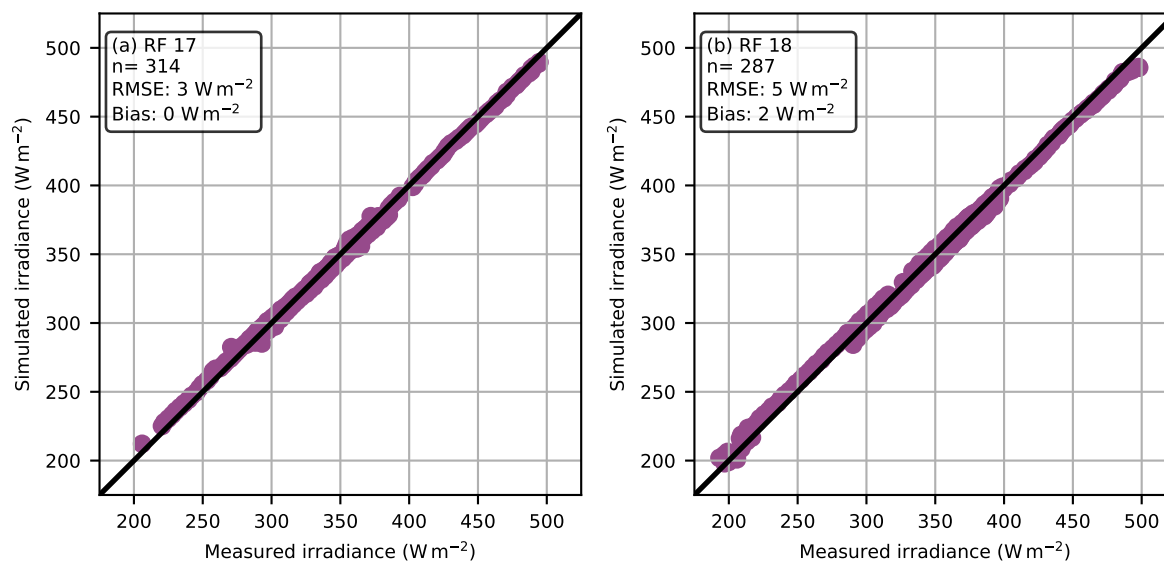
Figure 6. Scatter plot of minutely mean BACARDI measured diffuse solar downward irradiance against ecRad simulations for times when HALO was above $11\,\mathrm{km}$ altitude for (a) RF 17 and (b) RF 18. The 1:1 line is shown in black.

below-cloud simulations at flight level. The solar transmissivity is chosen as a measure that compensates for the dominating effect of the solar zenith angle.

Figure 7 shows the distributions of solar transmissivity below cloud from the ecRad simulations compared to the temporally averaged BACARDI measurements with the mean depicted as the dashed line. RF 17 is characterized by higher transmissivities

295 (mean value of 0.88) compared to RF 18 (mean value of 0.58). This is in line with the geometrically and optically thin cirrus observed in RF 17 compared to the geometrically and optically thicker cirrus of RF 18. However, for RF 17 the simulations show a mean transmissivity of 0.78 and do not reproduce this high transmissivity of the measurements. Switching the ice optics parameterization to either Yi2013 or Baran2016 improves the agreement slightly by increasing the mean values to 0.79 and 0.81 respectively. The same holds for RF 18 but the differences between the simulations and measurements are below 0.02.

300 Another difference is the width of the distribution, which does not match as well for RF 18 as for RF 17. Thus, although the mean transmissivity matches better, the simulations do not represent the whole width of the measured range for RF 18. The choice of ice optics parameterization can, therefore, not fully explain the difference between observations and the reference IFS-ecRad simulation (Fu-IFS).

4.2.2 IWC input

305 The cirrus radiative properties are determined by the IWC and r_{eff}. To evaluate the contribution of IWC and r_{eff} as potential biases in the simulation of solar irradiance and cirrus transmissivity, the VarCloud estimated IWC and r_{eff} are used as inde-
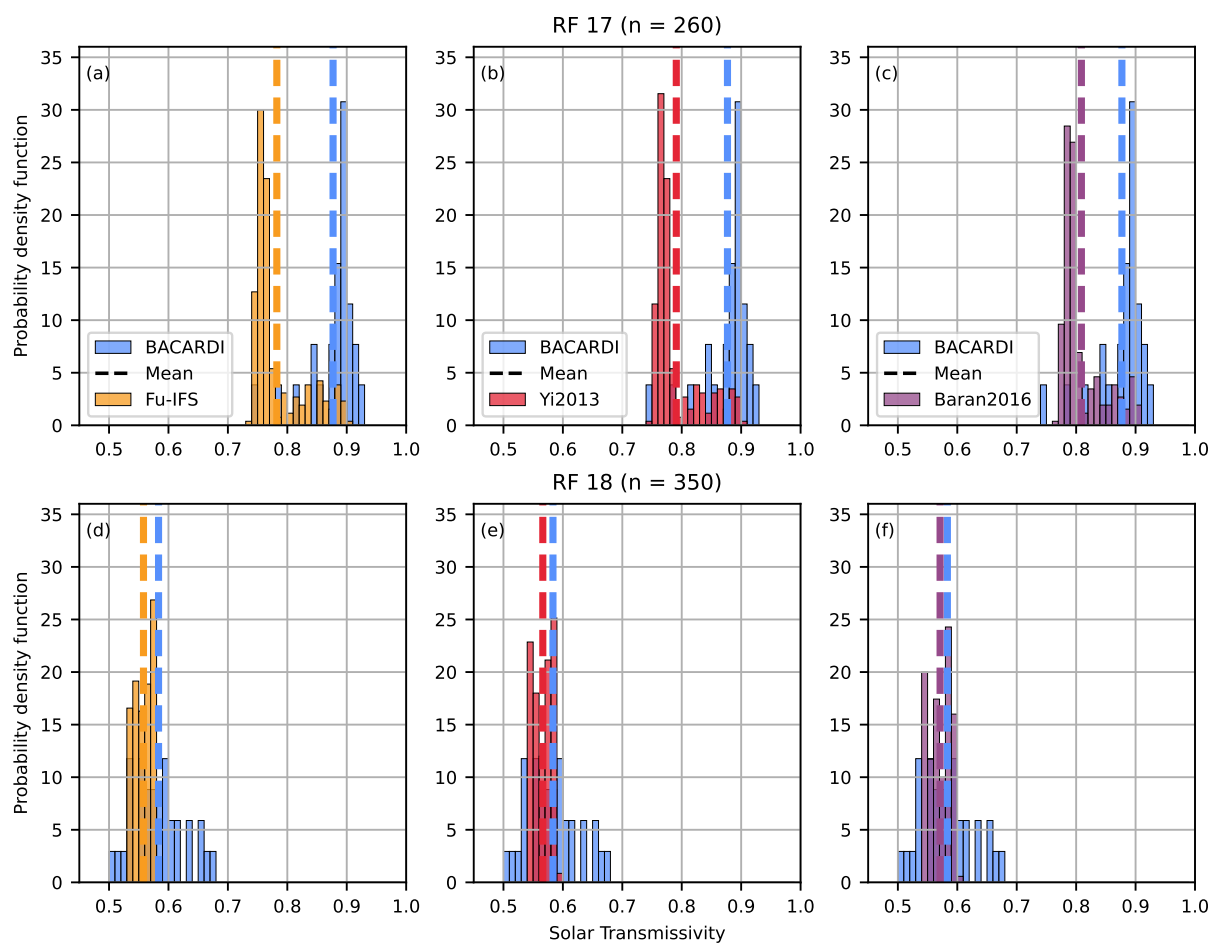
Figure 7. Histograms of solar transmissivity below cloud with bin size of 0.01 for (a - c) RF 17 and (d - f) RF 18. Each column compares the minutely averaged below-cloud BACARDI measurements with a simulation using a different ice optics parameterization: (a, d) Fu-IFS, (b, e) Yi2013 and (c, f) Baran2016. The number of samples n is shown in the row title.
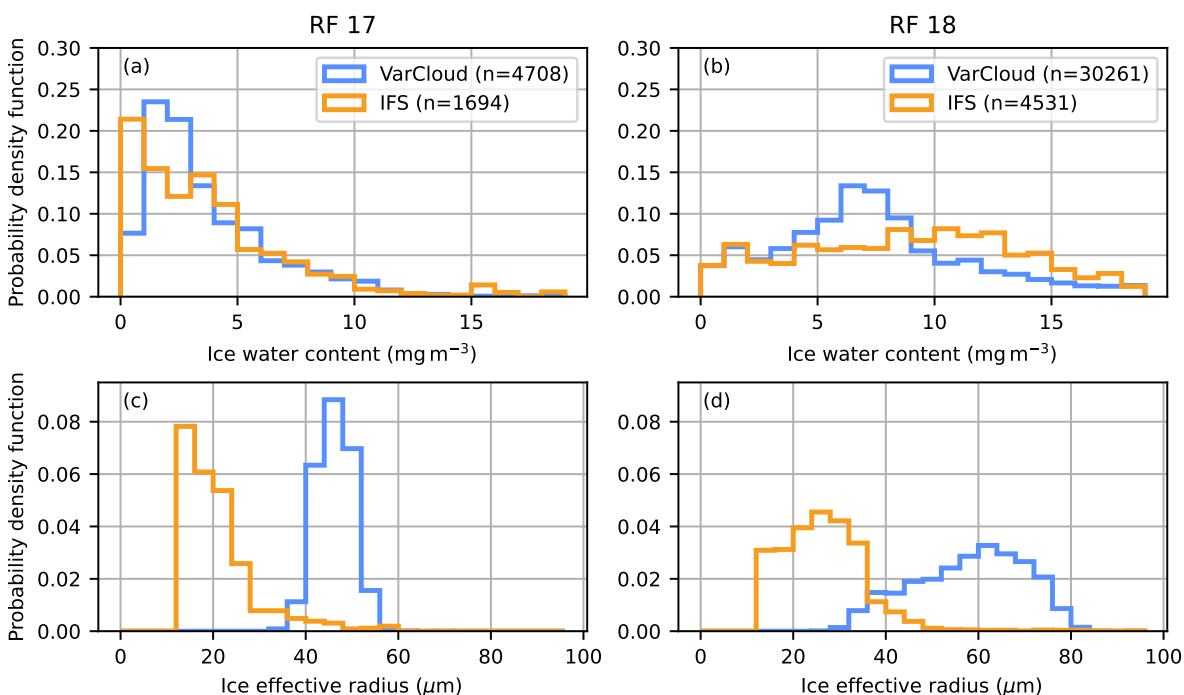
Figure 8. Probability density functions of (a, b) IWC with $1\,\mathrm{mg\,m^{-3}}$ binwidth and (c, d) r_{eff} with $4\,\mathrm{\mu m}$ binwidth for (a, c) RF 17 and (b, d) RF 18 of the IFS/parameterization output from the below-cloud section and the VarCloud retrieval. n depicts the number of points used in each histogram.

pendent measures. The probability density functions of the predicted IWC and r_{eff} for the below-cloud sections of RF 17 and RF 18 and the retrieved values from the above-cloud sections are shown in Fig. 8. Due to the temporal resolution of VarCloud, more points are available for the retrieval compared to the IFS. The distributions for the IWC look rather similar with the major

310   difference that the IFS shows more smaller values in the $0-1\,\mathrm{mg\,m^{-3}}$ bin for RF 17, whereas the VarCloud data has a peak at the $1-2\,\mathrm{mg\,m^{-3}}$ and $2-3\,\mathrm{mg\,m^{-3}}$ bin. Both distribution for RF 17 are positively skewed. For RF 18 the distributions are flatter and show more large values than observed in RF 17. The VarCloud values show a flat peak at the $6-8\,\mathrm{mg\,m^{-3}}$ bins, whereas the IFS data do not show a very distinct peak at all. However, the IFS shows more large values. A more pronounced difference can be observed for r_{eff} where the Sun (2001) parameterization in the IFS predicts smaller particles with a mean of

315    $21.1\,\mathrm{\mu m}$ for RF 17 and $26.7\,\mathrm{\mu m}$ for RF 18 compared to the retrieved r_{eff} from VarCloud showing a mean of $46.3\,\mathrm{\mu m}$ for RF 17 and $57.9\,\mathrm{\mu m}$ for RF 18. The shape of the distributions is hereby similar.

As r_{eff} effects the optical properties of the cirrus, e.g., a smaller r_{eff} will result in a higher cloud optical thickness for the same IWC, these differences suggest that the IFS might overestimate the cirrus optical thickness. To test this hypothesis, a sensitivity study is conducted, in which the IWC and r_{eff} retrieved by VarCloud are used as input for ecRad simulations of

320   the below-cloud section. For this test, the full temporal resolution of the remote sensing observations is used, as the test is
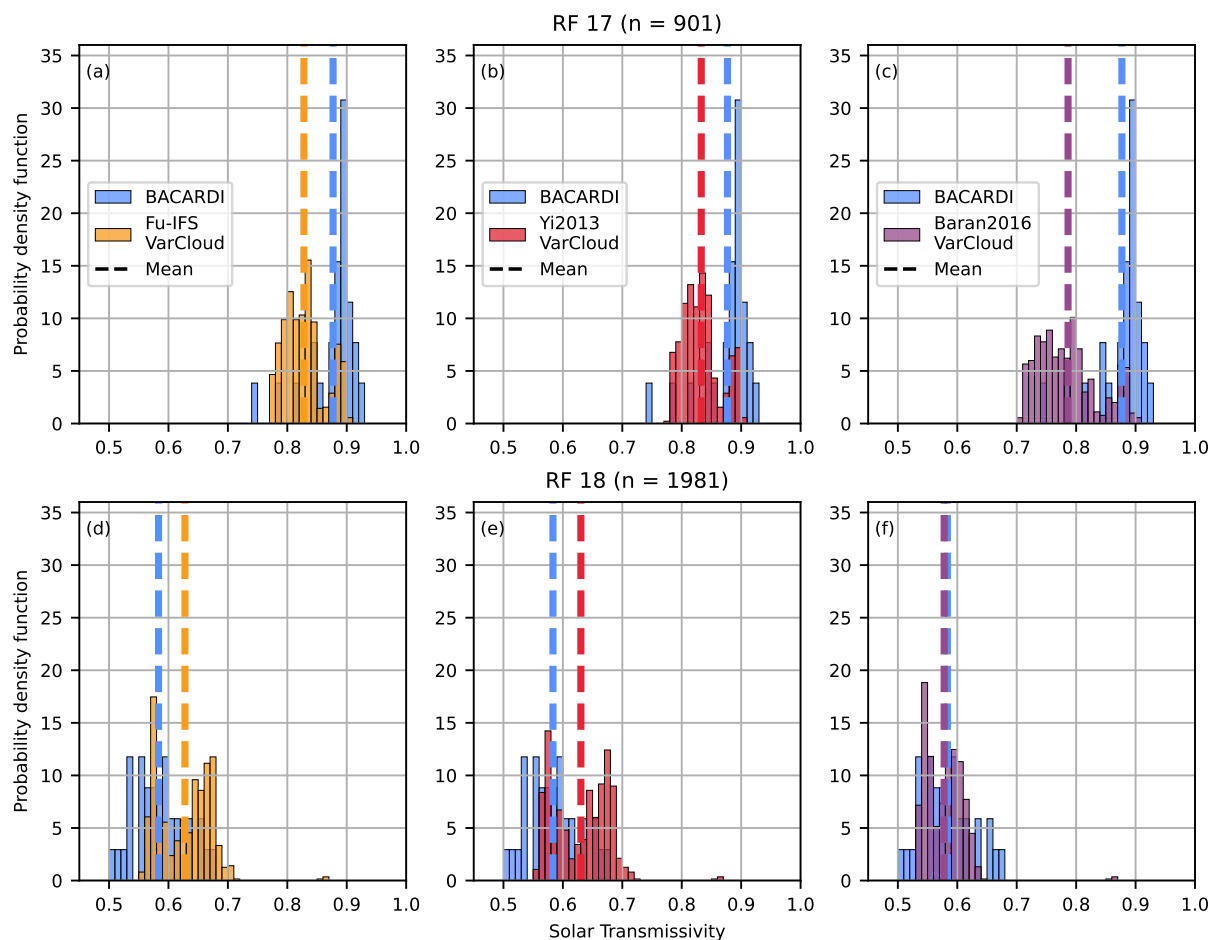
Figure 9. As Fig. 7 but using the VarCloud retrieved IWC and r_{eff} as input for the ecRad simulations. Both BACARDI and ecRad data are calculated for 1 Hz frequency.

not restricted to the IFS grid box size. To better compare the simulations, the vertical resolution of VarCloud is interpolated onto the IFS vertical resolution. Since the VarCloud retrieval represents the actual heterogeneity of the cloud, there is no need to introduce any sub-grid variability. Thus, the value of the fractional standard deviation (`fractional_std`) is set to 0. It describes the horizontal variability of the cloud water content in a model layer (ecRad documentation website) and is set to 1 in

325   the IFS and in the simulations shown in the previous section. The VarCloud simulations are also done with the three available ice optics parameterizations. However, since Baran2016 does not use the r_{eff} as a direct input only the retrieved IWC is used in these simulations.

     Figure 9 shows the result of the VarCloud-driven ecRad simulations using the three different ice optics parameterization Fu-IFS, Yi2013 and Baran2016 compared to the BACARDI measurements. Compared to the IFS-driven simulations, the mean

330   solar transmissivity is closer to the measured one for RF 17 using the operational Fu-IFS (0.83) and the experimental Yi2013

(0.83) ice optics parameterization. For Baran2016 the cloud is simulated as optically thicker than before, leading to a lower mean transmissivity of 0.79. For RF 18, Fu-IFS and Yi2013 overestimate the solar transmissivity by 0.05, whereas Baran2016 matches the mean transmissivity of 0.58 perfectly. The main reason for these changes is the larger r_{eff} retrieved with VarCloud. Larger ice crystals at a similar IWC result in fewer ice crystals, which in turn leads to less scattering and therefore higher

335   transmissivity of the cirrus. Since Baran2016 does not use r_{eff} as input, the difference to the IFS-driven simulation is smaller as it is solely caused by the difference in IWC between the IFS and VarCloud. As shown in Fig. 8 this difference is larger for RF 17 with more small values of IWC which in this case leads to an optically thicker cloud.

Table 2 summarizes the mean solar transmissivity calculated with the BACARDI measurements and with the different ecRad setups. It can be seen that for the IFS-driven simulations, the choice of ice optics parameterization does not change the result

340   significantly. However, with the VarCloud input, the difference between Fu-IFS/Yi2013 and Baran2016 becomes larger. This indicates, that the r_{eff} parameterization and the underestimation of r_{eff} by it is the cause for this difference.

Table 2. Mean solar transmissivity calculated with the BACARDI measurements (bold) and all ecRad simulations using different input and different ice optics parameterizations.

Input	Ice Optics Parameterization	Mean Transmissivity	
		RF 17	RF 18
BACARDI		**0.88**	**0.58**
IFS	Fu-IFS	0.78	0.56
	Yi2013	0.79	0.57
	Baran2016	0.81	0.57
VarCloud	Fu-IFS	0.83	0.63
	Yi2013	0.83	0.63
	Baran2016	0.79	0.58

To better understand why r_{eff} is so important in these cases the optical depth resulting from the IWC and r_{eff} is calculated. As the incident wavelength is small compared to the ice crystal size in the solar part of the spectrum, the geometric optic assumption holds and the extinction coefficient β_{ext} can be calculated following Francis et al. (1994) with:

345    $$\beta_{\text{ext}} = \frac{3}{2} \frac{\text{IWC}}{\rho_{\text{ice}} \cdot r_{\text{eff}}} \tag{1}$$

with $\rho_{\text{ice}} = 916.7 \, \text{kg m}^{-3}$ being the density of ice. Vertically integrating β_{ext} over the whole cloud results in the optical depth. This is the primary variable influencing the transmissivity and using the IFS predicted values of IWC and r_{eff} to calculate it results in a mean optical depth of 0.42 with a standard deviation of 0.17 for RF 17 and 1.9 (0.36) for RF 18. Using the VarCloud retrieved values instead leads to lower optical depths for both cases with 0.27 (0.24) for RF 17 and 1.14 (0.52) for

350   RF 18. This explains why the simulations with Fu-IFS and Yi2013 produce higher transmissivities for both cases when using

the VarCloud retrieval as input. However, even though the performance of ecRad is improved for RF 17 some radiative effects are still missing in the simulation. 3D radiative effects play a more important role at high solar zenith angles and could explain some of the difference. The VarCloud-driven simulations for RF 18 result in an overestimation of solar transmissivity for the Fu-IFS and Yi2013 ice optics parameterization caused by the larger r_{eff}. It has to be mentioned here that also the retrieval is based on assumptions of particle habit and as such is not perfect. Thus, some of the difference can be explained by the retrieval uncertainty of r_{eff}.

4.2.3 Sea ice albedo influence

A crucial parameter determining the radiative transfer in the Arctic is the sea ice. Our case studies were situated in latitudes close to $80°$ N over closed sea ice with only small ridges, leads and refrozen leads visible from the aircraft. These relatively small inhomogeneities of the sea ice are only represented in the sea ice fraction of IFS for RF 17, where it is between 0.989 and 0.999 in the area of the case studies. For RF 18 it is constantly 1. Although, the inhomogeneities are not imprinted in the time series of irradiance as they smooth out due to the large field of view of BACARDI in high altitude (Jäkel et al., 2013), the mean surface albedo might be reduced compared to a $100\,\%$ closed sea ice cover. A direct comparison between the IFS climatological spectral sea ice albedo and the measured one is not possible as the BACARDI measurements can only be used to derive the broadband albedo. However, the comparison of the broadband albedo also needs to consider that the BACARDI measurements provide a sea ice albedo for cloudy diffuse illumination conditions, which the IFS sea ice albedo parameterization does account for but uses constant values for the diffuse albedo. The IFS predicts a nearly constant broadband albedo of 0.76 for both RF 17 and RF 18, whereas the BACARDI derived below-cloud broadband albedo ranges from 0.6 to 0.89 for RF 17 and 0.71 to 0.93 for RF 18. The observed mean albedo value for RF 17 (0.72) is thus lower than the albedo assumed in the IFS, while for RF 18 (0.82) the albedo is underestimated by the IFS.

To investigate the influence of this mismatch, two more simulations are performed, in which the spectral albedo provided by the parameterization from Ebert and Curry (1993) is scaled with the measured broadband albedo from BACARDI. For these simulations the Fu-IFS ice optics parameterization is used. The mean solar transmissivity below cloud is reduced from 0.78 in the reference case to 0.77 for RF 17 and from 0.56 to 0.54 for RF 18. As this change is minute and also in the wrong direction the sea ice albedo representation in the IFS does not seem to be the major problem for these cases.

5 Summary and Conclusions

This study evaluated the accuracy of the IFS to simulate optical and microphysical properties of Arctic cirrus. Airborne measurements of cirrus transmissivity of two cirrus cases, one optically thin and one optically thick, were compared to offline radiative transfer simulations by ecRad initialized with IFS forecasts. The standard IFS/ecRad configuration showed lower cirrus transmissivity compared to the observations for the optically thin cirrus. For optically thick cirrus only slight differences were observed. We investigated the influence of different ice optics parameterizations available within ecRad, namely the operational Fu-IFS, and the two experimental ones Yi2013 and Baran2016.

Judging from the results of this case study, a change in ice optics parameterization does not result in better model performance. Instead, cloud microphysical properties were found to be a possible reason for the mismatch. Replacing both the IWC

385   and r_{eff} with retrieved values based on active remote sensing measurements on HALO can improve the match between the measured solar transmissivity and the simulations for RF 17. This holds for operating ecRad with the Fu-IFS and the Yi2013 ice optics parameterization. When using Baran2016, where only the IWC can be replaced with the retrieved values, the differences increased. For the optically thick cirrus of RF 18 this sensitivity test causes an overestimation of the solar transmissivity when using Fu-IFS and Yi2013, whereas it causes a slightly better match for Baran2016. This indicates that the IWC forecasted

390   by the IFS is realistic and the main reason for the mismatch between the simulated and measured solar transmissivities is the r_{eff} assumption, either given by the parameterization from Sun (2001) or encoded within Baran2016.

Although not significantly improving performance, moving to a new ice optics parameterization such as the one from Baran et al. (2016) has other positive side effects. First, the parameterization is based on more recent in situ measurements of ice crystals and uses a parameterization by Field et al. (2007) to generate PSDs across a wide range of temperature and IWC

395   values. This improves the statistical basis of the parameterization and makes it more likely to be valid for the Arctic. Second, the Baran2016 parameterization removes the dependence on the r_{eff} parameterization from Sun (2001). The Sun (2001) parameterization is based on the PSD parameterization developed by McFarquhar and Heymsfield (1997), which they derived from measurements in the Tropics during the Central Equatorial Pacific EXperiment (CEPEX). Thus, the measurement data used may not be representative of the mid-latitudes or the Arctic. To account for the observation that ice crystals measured in

400   the tropics are generally larger than the ones in the mid-latitudes, a cosine weighting depending on the latitude is included in the IFS's definition of the minimum r_{eff}. This makes sure that with increasing latitude the minimum r_{eff} decreases. However, recent in situ observations presented by De La Torre Castro et al. (2023) show, that the size of ice crystals in Arctic cirrus is on average larger than in the mid-latitudes. The cosine weighting only affects the lower bound of r_{eff}. Nonetheless, due to the IWC predicted by the IFS and the underlying in situ data of the parameterization, larger particle sizes are not predicted under

405   Arctic conditions.

RF 17 shows an optically thin cirrus, which was highly transmissive for solar radiation. This transmissivity could not be reproduced with the simulations. Thus, another factor is missing in the simulation that would be able to increase the transmissivity. At such high solar zenith angles, 3D effects become of more importance but are ignored in the operational setup of ecRad. Recent work tries to parameterize these 3D effects within ecRad (Hogan et al., 2019). Simulations with these parame-

410   terizations turned on, however, do not yield improved results (not shown).

Finally, more in situ measurements of the PSD of Arctic cirrus are needed to further improve our understanding of the regional microphysical differences of cirrus and to properly represent these differences in ice optics parameterizations.

Code and data availability. A repository with a Fortran namelist detailing the ecRad setup, a sample input file and the python code for the figures is available on GitHub, last accessed 02.02.2024. The BACARDI data (Luebke et al., 2023) and the HAMP data (Dorff et al.,

415   2023) are available via Pangaea. The basic HALO data (altitude, true air speed, location, . . .) and the WALES data are available via the

HALO Database. The dropsonde data is under final quality control and will be published on PANGAEA. The VarCloud retrieval is available upon request. The IFS output used in this study was downloaded directly from the ECMWF servers using the Meteorological Archival and Retrieval System (registration required). The trace gas data used in the ecRad simulations is available at the ecRad documentation website.

Author contributions. JR performed the analysis, the radiative transfer simulations, and drafted and finalized the manuscript. AE and MW
420 contributed to the conception and the design of the study. HM contributed to the setup of the radiative transfer simulations. FE performed the VarCloud retrieval and contributed to the design of the radiative transfer simulations. BK performed the trajectory calculations. All authors contributed to the discussion of the results. All authors reviewed the manuscript.

Competing interests. The authors declare no competing interests.

Acknowledgements. We thank Kevin Wolf for a fruitful discussion and proof reading the manuscript. We thank the whole HALO-(AC)[3]
425 team for making the campaign possible and Geet George for the processing of the dropsonde data. We gratefully acknowledge the funding by the Deutsche Forschungsgemeinschaft (DFG, German Research Foundation) – Project Number 268020496 – TRR 172, within the Transregional Collaborative Research Center "ArctiC Amplification: Climate Relevant Atmospheric and SurfaCe Processes, and Feedback Mechanisms (AC)3". We are further grateful for funding of project grant no. 316646266 by the Deutsche Forschungsgemeinschaft (DFG, German Research Foundation) within the framework of Priority Programme SPP 1294 to promote research with HALO. We thank Matthew
430 A. Petroff for providing freely available scientific colormaps, enhancing the visual quality of this work (Petroff, 28 December 2021). Parts of the results in this work make use of the colormaps in the CMasher package (Van Der Velden, 2020).

References

Baran, A. J.: From the single-scattering properties of ice crystals to climate prediction: A way forward, Atmos. Res., 112, 45–69, https://doi.org/10.1016/j.atmosres.2012.04.010, 2012.

435 Baran, A. J. and Labonnote, L.-C.: A self-consistent scattering model for cirrus. I: The solar region, Q. J. Roy. Meteor. Soc., 133, 1899–1912, https://doi.org/10.1002/qj.164, 2007.

Baran, A. J., Hill, P., Furtado, K., Field, P., and Manners, J.: A Coupled Cloud Physics–Radiation Parameterization of the Bulk Optical Properties of Cirrus and Its Impact on the Met Office Unified Model Global Atmosphere 5.0 Configuration, J. Climate, 27, 7725–7752, https://doi.org/10.1175/JCLI-D-13-00700.1, 2014.

440 Baran, A. J., Hill, P., Walters, D., Hardiman, S. C., Furtado, K., Field, P. R., and Manners, J.: The Impact of Two Coupled Cirrus Micro-physics–Radiation Parameterizations on the Temperature and Specific Humidity Biases in the Tropical Tropopause Layer in a Climate Model, J. Climate, 29, 5299–5316, https://doi.org/10.1175/jcli-d-15-0821.1, 2016.

Baum, B. A., Yang, P., Heymsfield, A. J., Schmitt, C. G., Xie, Y., Bansemer, A., Hu, Y.-X., and Zhang, Z.: Improvements in Short-wave Bulk Scattering and Absorption Models for the Remote Sensing of Ice Clouds, J. Appl. Meteorol. Clim., 50, 1037–1056,
445 https://doi.org/10.1175/2010JAMC2608.1, 2011.

Cariolle, D. and Déqué, M.: Southern hemisphere medium-scale waves and total ozone disturbances in a spectral general circulation model, J. Geophys. Res-Atmos., 91, 10 825–10 846, https://doi.org/10.1029/JD091iD10p10825, 1986.

Cariolle, D. and Teyssèdre, H.: A revised linear ozone photochemistry parameterization for use in transport and general circulation models: multi-annual simulations, Atmos. Chem. Phys., 7, 2183–2196, https://doi.org/10.5194/acp-7-2183-2007, 2007.

450 Cazenave, Q., Ceccaldi, M., Delanoë, J., Pelon, J., Groß, S., and Heymsfield, A.: Evolution of DARDAR-CLOUD ice cloud retrievals: new parameters and impacts on the retrieved microphysical properties, Atmos. Meas. Tech., 12, 2819–2835, https://doi.org/10.5194/amt-12-2819-2019, 2019.

De La Torre Castro, E., Jurkat-Witschas, T., Afchine, A., Grewe, V., Hahn, V., Kirschler, S., Krämer, M., Lucke, J., Spelten, N., Wernli, H., Zöger, M., and Voigt, C.: Differences in microphysical properties of cirrus at high and mid-latitudes, Atmos. Chem. Phys., 23, 13 167–
455 13 189, https://doi.org/10.5194/acp-23-13167-2023, publisher: Copernicus GmbH, 2023.

Delanoë, J. and Hogan, R. J.: A variational scheme for retrieving ice cloud properties from combined radar, lidar, and infrared radiometer, J. Geophys. Res-Atmos., 113, https://doi.org/10.1029/2007JD009000, 2008.

Delanoë, J., Protat, A., Testud, J., Bouniol, D., Heymsfield, A. J., Bansemer, A., Brown, P. R. A., and Forbes, R. M.: Statistical properties of the normalized ice particle size distribution, J. Geophys. Res-Atmos., 110, https://doi.org/10.1029/2004JD005405, 2005.

460 Dorff, H., Aubry, C., Ewald, F., Hirsch, L., Jansen, F., Konow, H., Mech, M., Ori, D., Ringel, M., Walbröl, A., Crewell, S., Ehrlich, A., Wendisch, M., and Ament, F.: Unified Airborne Active and Passive Microwave Measurements over Arctic Sea Ice and Ocean during the HALO-(AC)[3] Campaign in Spring 2022, PANGAEA [963250], https://doi.org/10.1594/PANGAEA.963250, 2023.

Ebert, E. E. and Curry, J. A.: A parameterization of ice cloud optical properties for climate models, J. Geophys. Res., 97, 3831, https://doi.org/10.1029/91jd02472, 1992.

465 Ebert, E. E. and Curry, J. A.: An intermediate one-dimensional thermodynamic sea ice model for investigating ice-atmosphere interactions, J. Geophys. Res. Oceans, 98, 10 085–10 109, https://doi.org/10.1029/93JC00656, 1993.

ecRad documentation website: ECMWF Radiation Scheme Home, https://confluence.ecmwf.int/display/ECRAD, last access: 31 January 2024.

Ehrlich, A., Zöger, M., Giez, A., Nenakhov, V., Mallaun, C., Maser, R., Röschenthaler, T., Luebke, A. E., Wolf, K., Stevens, B., and Wendisch,
470   M.: A new airborne broadband radiometer system and an efficient method to correct dynamic thermal offsets, Atmos. Meas. Tech., 16,
       1563–1581, https://doi.org/10.5194/amt-16-1563-2023, 2023.

Eichler, H., Ehrlich, A., Wendisch, M., Mioche, G., Gayet, J.-F., Wirth, M., Emde, C., and Minikin, A.: Influence of ice crystal shape on
       retrieval of cirrus optical thickness and effective radius: A case study, J. Geophys. Res., 114, https://doi.org/10.1029/2009jd012215, 2009.

Ewald, F., Groß, S., Wirth, M., Delanoë, J., Fox, S., and Mayer, B.: Why we need radar, lidar, and solar radiance observations to constrain
475   ice cloud microphysics, Atmos. Meas. Tech., 14, 5029–5047, https://doi.org/10.5194/amt-14-5029-2021, publisher: Copernicus GmbH,
       2021.

Field, P. R., Heymsfield, A. J., and Bansemer, A.: Snow Size Distribution Parameterization for Midlatitude and Tropical Ice Clouds, J. Atmos.
       Sci., 64, 4346–4365, https://doi.org/10.1175/2007jas2344.1, 2007.

Flemming, J., Benedetti, A., Inness, A., Engelen, R. J., Jones, L., Huijnen, V., Remy, S., Parrington, M., Suttie, M., Bozzo, A., Peuch, V.-H.,
480   Akritidis, D., and Katragkou, E.: The CAMS interim Reanalysis of Carbon Monoxide, Ozone and Aerosol for 2003–2015, Atmos. Chem.
       Phys., 17, 1945–1983, https://doi.org/10.5194/acp-17-1945-2017, 2017.

Foot, J. S.: Some observations of the optical properties of clouds. II: Cirrus, Q. J. Roy. Meteor. Soc., 114, 145–164,
       https://doi.org/10.1002/qj.49711447908, 1988.

Francis, P. N., Jones, A., Saunders, R. W., Shine, K. P., Slingo, A., and Sun, Z.: An observational and theoretical study of the radiative
485   properties of cirrus: Some results from ICE'89, Q. J. Roy. Meteor. Soc., 120, 809–848, https://doi.org/10.1002/qj.49712051804, 1994.

Fu, Q.: An Accurate Parameterization of the Solar Radiative Properties of Cirrus Clouds for Climate Models, J. Climate, 9, 2058–2082,
       https://doi.org/10.1175/1520-0442(1996)009<2058:aapots>2.0.co;2, 1996.

Fu, Q.: A New Parameterization of an Asymmetry Factor of Cirrus Clouds for Climate Models, J. Atmos. Sci., 64, 4140–4150,
       https://doi.org/10.1175/2007JAS2289.1, 2007.

490   Fu, Q., Yang, P., and Sun, W. B.: An Accurate Parameterization of the Infrared Radiative Properties of Cirrus Clouds for Climate Models, J.
       Climate, 11, 2223–2237, https://doi.org/10.1175/1520-0442(1998)011<2223:aapoti>2.0.co;2, 1998.

HALO Database: The High Altitude and LOng Range Research Aircraft Database, https://halo-db.pa.op.dlr.de/mission/130, last access: 31
       January 2024.

Hersbach, H., Bell, B., Berrisford, P., Hirahara, S., Horányi, A., Muñoz-Sabater, J., Nicolas, J., Peubey, C., Radu, R., Schepers, D., Simmons,
495   A., Soci, C., Abdalla, S., Abellan, X., Balsamo, G., Bechtold, P., Biavati, G., Bidlot, J., Bonavita, M., Chiara, G., Dahlgren, P., Dee, D.,
       Diamantakis, M., Dragani, R., Flemming, J., Forbes, R., Fuentes, M., Geer, A., Haimberger, L., Healy, S., Hogan, R. J., Hólm, E.,
       Janisková, M., Keeley, S., Laloyaux, P., Lopez, P., Lupu, C., Radnoti, G., Rosnay, P., Rozum, I., Vamborg, F., Villaume, S., and Thépaut,
       J.: The ERA5 global reanalysis, Q. J. Roy. Meteor. Soc., 146, 1999–2049, https://doi.org/10.1002/qj.3803, 2020.

Heymsfield, A. J., Schmitt, C., and Bansemer, A.: Ice Cloud Particle Size Distributions and Pressure-Dependent Terminal Velocities from In
500   Situ Observations at Temperatures from 0° to -86°C, J. Atmos. Sci., 70, 4123–4154, https://doi.org/10.1175/JAS-D-12-0124.1, 2013.

Hogan, R. J.: Fast Lidar and Radar Multiple-Scattering Models. Part I: Small-Angle Scattering Using the Photon Variance–Covariance
       Method, J. Atmos. Sci., 65, 3621–3635, https://doi.org/10.1175/2008JAS2642.1, 2008.

Hogan, R. J. and Bozzo, A.: A Flexible and Efficient Radiation Scheme for the ECMWF Model, J. Adv. Model. Earth Syst., 10, 1990–2008,
       https://doi.org/10.1029/2018ms001364, 2018.

505 Hogan, R. J., Tian, L., Brown, P. R. A., Westbrook, C. D., Heymsfield, A. J., and Eastment, J. D.: Radar Scattering from Ice Aggregates Using the Horizontally Aligned Oblate Spheroid Approximation, J. Appl. Meteorol. Clim., 51, 655–671, https://doi.org/10.1175/JAMC-D-11-074.1, 2012.

Hogan, R. J., Schäfer, S. A. K., Klinger, C., Chiu, J. C., and Mayer, B.: Representing 3-D cloud radiation effects in two-stream schemes: 2. Matrix formulation and broadband evaluation, J. Geophys. Res-Atmos., 121, 8583–8599, https://doi.org/10.1002/2016JD024875, 2016.

510 Hogan, R. J., Fielding, M. D., Barker, H. W., Villefranque, N., and Schäfer, S. A. K.: Entrapment: An Important Mechanism to Explain the Shortwave 3D Radiative Effect of Clouds, J. Atmos. Sci., 2019, 48–66, https://doi.org/10.1175/JAS-D-18-0366.1, 2019.

Hong, Y. and Liu, G.: The Characteristics of Ice Cloud Properties Derived from CloudSat and CALIPSO Measurements, J. Climate, 28, 3880–3901, https://doi.org/10.1175/jcli-d-14-00666.1, 2015.

Inness, A., Baier, F., Benedetti, A., Bouarar, I., Chabrillat, S., Clark, H., Clerbaux, C., Coheur, P., Engelen, R. J., Errera, Q., Flemming, J.,
515 George, M., Granier, C., Hadji-Lazaro, J., Huijnen, V., Hurtmans, D., Jones, L., Kaiser, J. W., Kapsomenakis, J., Lefever, K., Leitão, J., Razinger, M., Richter, A., Schultz, M. G., Simmons, A. J., Suttie, M., Stein, O., Thépaut, J.-N., Thouret, V., Vrekoussis, M., Zerefos, C., and the MACC team: The MACC reanalysis: an 8 yr data set of atmospheric composition, Atmos. Chem. Phys., 13, 4073–4109, https://doi.org/10.5194/acp-13-4073-2013, 2013.

Jäkel, E., Wendisch, M., and Mayer, B.: Influence of spatial heterogeneity of local surface albedo on the area-averaged surface albedo
520 retrieved from airborne irradiance measurements, Atmos. Meas. Tech., 6, 527–537, https://doi.org/10.5194/amt-6-527-2013, 2013.

Järvinen, E., Jourdan, O., Neubauer, D., Yao, B., Liu, C., Andreae, M. O., Lohmann, U., Wendisch, M., McFarquhar, G. M., Leisner, T., and Schnaiter, M.: Additional global climate cooling by clouds due to ice crystal complexity, Atmos. Chem. Phys., 18, 15 767–15 781, https://doi.org/10.5194/acp-18-15767-2018, 2018.

Kopp, G. and Lean, J. L.: A new, lower value of total solar irradiance: Evidence and climate significance, Geophys. Res. Lett., 38,
525 https://doi.org/10.1029/2010GL045777, 2011.

Krämer, M., Rolf, C., Spelten, N., Afchine, A., Fahey, D., Jensen, E., Khaykin, S., Kuhn, T., Lawson, P., Lykov, A., Pan, L. L., Riese, M., Rollins, A., Stroh, F., Thornberry, T., Wolf, V., Woods, S., Spichtinger, P., Quaas, J., and Sourdeval, O.: A microphysics guide to cirrus - Part 2: Climatologies of clouds and humidity from observations, Atmos. Chem. Phys., 20, 12 569–12 608, https://doi.org/10.5194/acp-20-12569-2020, 2020.

530 Lawson, R. P., Woods, S., Jensen, E., Erfani, E., Gurganus, C., Gallagher, M., Connolly, P., Whiteway, J., Baran, A. J., May, P., Heymsfield, A., Schmitt, C. G., McFarquhar, G., Um, J., Protat, A., Bailey, M., Lance, S., Muehlbauer, A., Stith, J., Korolev, A., Toon, O. B., and Krämer, M.: A Review of Ice Particle Shapes in Cirrus formed In Situ and in Anvils, J. Geophys. Res. Atmos., 124, 10 049–10 090, https://doi.org/10.1029/2018jd030122, 2019.

Light, B., Smith, M. M., Perovich, D. K., Webster, M. A., Holland, M. M., Linhardt, F., Raphael, I. A., Clemens-Sewall, D., Macfarlane,
535 A. R., Anhaus, P., and Bailey, D. A.: Arctic sea ice albedo: Spectral composition, spatial heterogeneity, and temporal evolution observed during the MOSAiC drift, Elementa: Science of the Anthropocene, 10, https://doi.org/10.1525/elementa.2021.000103, 2022.

Liou, K.-N.: Influence of Cirrus Clouds on Weather and Climate Processes: A Global Perspective, Mon. Weather Rev., 114, 1167–1199, https://doi.org/10.1175/1520-0493(1986)114<1167:ioccow>2.0.co;2, 1986.

Luebke, A. E., Avallone, L. M., Schiller, C., Meyer, J., Rolf, C., and Krämer, M.: Ice water content of Arctic, midlatitude, and tropical
540 cirrus – Part 2: Extension of the database and new statistical analysis, Atmos. Chem. Phys., 13, 6447–6459, https://doi.org/10.5194/acp-13-6447-2013, 2013.

Luebke, A. E., Ehrlich, A., Röttenbacher, J., Zöger, M., Giez, A., Nenakhov, V., Mallaun, C., and Wendisch, M.: Broadband solar and terrestrial, upward and downward irradiance measured by BACARDI on HALO during the HALO-(AC)[3] field campaign in 2022, PANGAEA [963739], https://doi.org/10.1594/PANGAEA.963739, 2023.

545 Lynch, D. K., ed.: Cirrus, Oxford University Press, 2002.

Marsing, A., Meerkötter, R., Heller, R., Kaufmann, S., Jurkat-Witschas, T., Krämer, M., Rolf, C., and Voigt, C.: Investigating the radiative effect of Arctic cirrus measured in situ during the winter 2015–2016, Atmos. Chem. Phys., 23, 587–609, https://doi.org/10.5194/acp-23-587-2023, 2023.

McFarquhar, G. M.: Comments on 'Parametrization of effective sizes of cirrus-cloud particles and its verification against ob-
550 servations' by Zhian Sun and Lawrie Rikus. October B, 1999,125, 3037–3055, Q. J. Roy. Meteor. Soc., 127, 261–265, https://doi.org/10.1002/qj.49712757115, 2001.

McFarquhar, G. M. and Heymsfield, A. J.: Parameterization of Tropical Cirrus Ice Crystal Size Distributions and Implications for Radiative Transfer: Results from CEPEX, J. Atmos. Sci., 54, 2187–2200, https://doi.org/10.1175/1520-0469(1997)054<2187:potcic>2.0.co;2, 1997.

Mech, M., Orlandi, E., Crewell, S., Ament, F., Hirsch, L., Hagen, M., Peters, G., and Stevens, B.: HAMP – the microwave package on the
555 High Altitude and LOng range research aircraft (HALO), Atmos. Meas. Tech., 7, 4539–4553, https://doi.org/10.5194/amt-7-4539-2014, 2014.

Mishchenko, M. I., Travis, L. D., and Mackowski, D. W.: T-matrix computations of light scattering by nonspherical particles: A review, J. Quant. Spectrosc. Ra., 55, 535–575, https://doi.org/10.1016/0022-4073(96)00002-7, 1996.

Mlawer, E. J., Taubman, S. J., Brown, P. D., Iacono, M. J., and Clough, S. A.: Radiative transfer for inhomoge-
560 neous atmospheres: RRTM, a validated correlated-k model for the longwave, J. Geophys. Res-Atmos., 102, 16663–16682, https://doi.org/https://doi.org/10.1029/97JD00237, 1997.

Müller, H., Ehrlich, A., Jäkel, E., Röttenbacher, J., Kirbus, B., Schäfer, M., Hogan, R. J., and Wendisch, M.: Evaluation of downward and upward solar irradiances simulated by the Integrated Forecasting System of ECMWF using airborne observations above Arctic low-level clouds, EGUsphere, pp. 1–28, https://doi.org/10.5194/egusphere-2023-2443, 2023.

565 Petroff, M. A.: Accessible Color Sequences for Data Visualization, arXiv [2107.02270], https://doi.org/10.48550/arXiv.2107.02270, 28 December 2021.

Pincus, R., Barker, H. W., and Morcrette, J.-J.: A fast, flexible, approximate technique for computing radiative transfer in inhomogeneous cloud fields, J. Geophys. Res-Atmos., 108, https://doi.org/10.1029/2002JD003322, 2003.

Schäfer, S. A. K., Hogan, R. J., Klinger, C., Chiu, J. C., and Mayer, B.: Representing 3-D cloud radiation effects in two-
570 stream schemes: 1. Longwave considerations and effective cloud edge length, J. Geophys. Res-Atmos., 121, 8567–8582, https://doi.org/10.1002/2016JD024876, 2016.

Sprenger, M. and Wernli, H.: The LAGRANTO Lagrangian analysis tool – version 2.0, Geosci. Model Dev., 8, 2569–2586, https://doi.org/10.5194/gmd-8-2569-2015, 2015.

Stevens, B., Ament, F., Bony, S., Crewell, S., Ewald, F., Gross, S., Hansen, A., Hirsch, L., Jacob, M., Kölling, T., Konow, H., Mayer, B.,
575 Wendisch, M., Wirth, M., Wolf, K., Bakan, S., Bauer-Pfundstein, M., Brueck, M., Delanoë, J., Ehrlich, A., Farrell, D., Forde, M., Gödde, F., Grob, H., Hagen, M., Jäkel, E., Jansen, F., Klepp, C., Klingebiel, M., Mech, M., Peters, G., Rapp, M., Wing, A. A., and Zinner, T.: A High-Altitude Long-Range Aircraft Configured as a Cloud Observatory: The NARVAL Expeditions, B. Am. Meteorol. Soc., 100, 1061–1077, https://doi.org/10.1175/bams-d-18-0198.1, 2019.

Sun, Z.: Reply to comments by Greg M. McFarquhar on 'Parametrization of effective sizes of cirrus-cloud particles and its verification against observations'. (October B, 1999,125, 3037–3055), Q. J. Roy. Meteor. Soc., 127, 267–271, https://doi.org/10.1002/qj.49712757116, 2001.

Sun, Z. and Rikus, L.: Parametrization of effective sizes of cirrus-cloud particles and its verification against observations, Q. J. Roy. Meteor. Soc., 125, 3037–3055, https://doi.org/10.1002/qj.49712556012, 1999.

Tang, G., Panetta, R. L., Yang, P., Kattawar, G. W., and Zhai, P.-W.: Effects of ice crystal surface roughness and air bubble inclusions on cirrus cloud radiative properties from remote sensing perspective, J. Quant. Spectrosc. Ra., 195, 119–131, https://doi.org/10.1016/j.jqsrt.2017.01.016, 2017.

Taylor, J. P., Edwards, J. M., Glew, M. D., Hignett, P., and Slingo, A.: Studies with a flexible new radiation code. II: Comparisons with aircraft short-wave observations, Q. J. Roy. Meteorol. Soc., 122, 839–861, https://doi.org/10.1002/qj.49712253204, 1996.

Van Der Velden, E.: CMasher: Scientific colormaps for making accessible, informative and 'cmashing' plots, Journal of Open Source Software, 5, 2004, https://doi.org/10.21105/joss.02004, 2020.

Várnai, T. and Davies, R.: Effects of Cloud Heterogeneities on Shortwave Radiation: Comparison of Cloud-Top Variability and Internal Heterogeneity, J. Atmos. Sci., 56, 4206–4224, https://doi.org/10.1175/1520-0469(1999)056<4206:EOCHOS>2.0.CO;2, 1999.

Wendisch, M., Müller, D., Schell, D., and Heintzenberg, J.: An Airborne Spectral Albedometer with Active Horizontal Stabilization, J. Atmos. Ocean. Tech., 18, 1856–1866, https://doi.org/10.1175/1520-0426(2001)018<1856:aasawa>2.0.co;2, 2001.

Wendisch, M., Pilewskie, P., Pommier, J., Howard, S., Yang, P., Heymsfield, A. J., Schmitt, C. G., Baumgardner, D., and Mayer, B.: Impact of cirrus crystal shape on solar spectral irradiance: A case study for subtropical cirrus, J. Geophys. Res. Atmos., 110, https://doi.org/10.1029/2004JD005294, 2005.

Wendisch, M., Yang, P., and Pilewskie, P.: Effects of ice crystal habit on thermal infrared radiative properties and forcing of cirrus, J. Geophys. Res. Atmos., 112, https://doi.org/10.1029/2006JD007899, 2007.

Wirth, M., Fix, A., Mahnke, P., Schwarzer, H., Schrandt, F., and Ehret, G.: The airborne multi-wavelength water vapor differential absorption lidar WALES: system design and performance, Appl. Phys. B, 96, 201–213, https://doi.org/10.1007/s00340-009-3365-7, 2009.

Wolf, K., Ehrlich, A., Mech, M., Hogan, R. J., and Wendisch, M.: Evaluation of ECMWF Radiation Scheme Using Aircraft Observations of Spectral Irradiance above Clouds, J. Atmos. Sci., 77, 2665–2685, https://doi.org/10.1175/jas-d-19-0333.1, 2020.

Wolf, V., Kuhn, T., Milz, M., Voelger, P., Krämer, M., and Rolf, C.: Arctic ice clouds over northern Sweden: microphysical properties studied with the Balloon-borne Ice Cloud particle Imager B-ICI, Atmos. Chem. Phys., 18, 17 371–17 386, https://doi.org/10.5194/acp-18-17371-2018, 2018.

Yang, P., Liou, K.-N., Bi, L., Liu, C., Yi, B., and Baum, B. A.: On the radiative properties of ice clouds: Light scattering, remote sensing, and radiation parameterization, Adv. Atmos. Sci., 32, 32–63, https://doi.org/10.1007/s00376-014-0011-z, 2014.

Yi, B.: Diverse cloud radiative effects and global surface temperature simulations induced by different ice cloud optical property parameterizations, Sci. Rep., 12, https://doi.org/10.1038/s41598-022-14608-w, publisher: Springer Science and Business Media LLC, 2022.

Yi, B., Yang, P., Baum, B. A., L'Ecuyer, T., Oreopoulos, L., Mlawer, E. J., Heymsfield, A. J., and Liou, K.-N.: Influence of Ice Particle Surface Roughening on the Global Cloud Radiative Effect, J. Atmos. Sci., 70, 2794–2807, https://doi.org/10.1175/jas-d-13-020.1, 2013.